Journal of Low Temperature Physics
https://doi.org/10.1007/s10909-022-02747-3

The Simulation and Design of an On-Chip Superconducting Millimetre Filter-Bank Spectrometer

G. Robson[1] · A. J. Anderson[3] · P. S. Barry[1,2,4] · S. Doyle[1] · K. S. Karkare[2,3]

Received: 1 November 2021 / Accepted: 4 May 2022
© The Author(s) 2022

Abstract
Superconducting on-chip filter banks provide a scalable, space saving solution to create imaging spectrometers at millimetre and submillimetre wavelengths. We present an easy to realise, lithographed superconducting filter design with a high tolerance to fabrication error. Using a capacitively coupled $\lambda/2$ microstrip resonator to define a narrow ($\lambda/\Delta\lambda = 300$) spectral pass band, the filtered output of a given spectrometer channel directly connects to a lumped-element kinetic inductance detector. We show the tolerance analysis of our design, demonstrating $< 11\%$ change in filter quality factor to any one realistic fabrication error and a full filter-bank efficiency forecast to be 50% after accounting for fabrication errors and dielectric loss tangent.

Keywords Millimetre wave · Spectrometry · On-chip filter bank · Superconductivity

1 Introduction

Millimetre wavelength astronomy contains a wealth of largely untapped information about the universe, ranging from measurements of the cosmic microwave background, to high redshift sources, to the inner workings of the dust-enshrouded regions of space. In the millimetre range, current, conventional spectrometer technology cannot scale up effectively to meet the sensitivity requirements for next-generation science cases. However, by capitalising on the small energy gap of superconductors, high sensitivity and ease of microwave circuit integration, superconducting filter-bank spectrometers (FBS) will be central in a range of future surveys in the millimetre region of the spectrum.

✉ G. Robson
RobsonG2@Cardiff.ac.uk

1 School of Physics and Astronomy, Cardiff University, Cardiff CF24 3AA, UK

2 Kavli Institute for Cosmological Physics, University of Chicago, Chicago, IL 60637, USA

3 Fermi National Accelerator Laboratory, Batavia, IL 60510, USA

4 High-Energy Physics Division, Argonne National Laboratory, Lemont, IL 60439, USA

Published online: 11 June 2022

FBS make use of the low-loss properties of superconductors operating well below the superconducting critical temperature (T_c), integrated microwave circuitry, and the sensitive and multiplexing capabilities of kinetic inductance detectors (KIDs) to create an efficient, compact and sensitive spectrometer that does not need large dispersive optical components, complex readout systems, or noise limiting amplifiers and local oscillators.

This paper presents a novel filter geometry with the application tailored to a medium-resolution mm-wave FBS, which to date has been demonstrated in two alternative instruments [1, 2]. This FBS is motivated by the SPT-SLIM project which is discussed in more detail in [3, 4]. Each filter bank will consist of 200 filter channels with a spectral resolution of $R = 300$ covering the 2 mm atmospheric transmission window (120–180 GHz).

2 On-Chip Filter-Bank Spectrometer Design

Incident light is coupled onto a transmission line via an antenna and guided to the filter bank. The filter bank is made up of a series of capacitively coupled half-wave ($\lambda/2$) resonators each with a different resonant frequency, f_0, set by the length, and spectral bandwidth, Δf, set by the coupling to the feedline.

The two key performance metrics of an on-chip spectrometer are the spectral resolution and the filter efficiency. The resolution, R, is equivalent to the quality factor, Q_{filt}, of each filter channel's resonator,

$$R = Q_{\text{filt}} = \frac{f_0}{\Delta f} \tag{1}$$

The filter efficiency is defined as the ratio of the total signal output through the channels to that coupled to the FBS. The maximum power transferred through the filter to the detector that can be achieved for a feedline filter T-junction such as this is 50% of the incident signal. Note that this is only the limit for a single filter; the overall FBS efficiency can exceed this with over-sampled filters [5].

3 Filter Geometry

The device will be built from a silicon on oxide (SOI) substrate (see Fig. 1) due to requirements for the architecture of the orthomode transducer (OMT) antennas and detectors. For further details, see [4]. Niobium is used for the feedline and filter structure since it is nearly lossless for the range of operation, due to its large superconducting gap.

A filter channel is created by coupling a $\lambda/2$ resonator to the main filter-bank feedline. On resonance, the current distribution results in a current node at each end of the resonator. This enables two coupling methods: inductively, by exploiting the current maximum in the centre as demonstrated by SuperSpec [1, 6]; or capacitively, using the voltage maximum at the ends, as seen in the DESHIMA

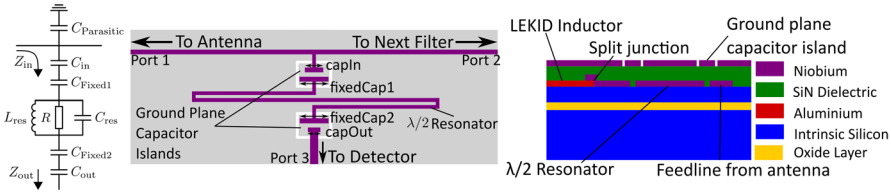

Fig. 1 (Color figure online) (Left) Lumped-element circuit diagram of the filter where the $\lambda/2$ resonator has been modelled as an LRC circuit with the resistor representing the loss mechanisms. (Centre) Top-down view of a filter channel microstrip geometry. (Right) Schematic of the SOI wafer structure in the region of a filter channel

[2, 7] device. Both examples tune the coupling quality factors, Q_C, via the separation between feedline and resonator. Due to fabrication tolerances, the tuning precision of Q_C is somewhat limited for such proximity couplings. We present an alternative coupling scheme that uses a pseudo-lumped-element capacitor island in the ground plane to form parallel plate capacitors, two at either end of the resonator, as shown in Fig. 1. This allows for a highly tuneable capacitive coupling using a microstrip architecture to minimise losses due to radiation [8].

The spectral resolution of a single channel can be written as the inverse sum of the quality factors due to losses within resonator, Q_{loss}, the coupling to the feedline, Q_{feed}, and detector coupling, Q_{det}, [1],

$$\frac{1}{R} = \frac{1}{Q_{filt}} = \frac{1}{Q_C} + \frac{1}{Q_{loss}} = \frac{1}{Q_{feed}} + \frac{1}{Q_{det}} + \frac{1}{Q_{loss}}. \tag{2}$$

Q_{feed} and Q_{det} can be controlled by changing the overlapping surface area of the parallel plates. For this design, Q_{filt} is largely controlled by the capacitor widths "capIn" and "capOut" [see Fig. and f_0 by the resonator length (see Fig. 1)]. Using Sonnet EM [9] to simulate the geometry in Fig. 1, for a variety of resonator lengths across the band, a simulation sweeping capIn values was carried out with the port 3 impedance set high enough to resemble an open circuit. Fitting Lorentzian curves, the capIn yielding a $Q_{feed} = 600$ can be interpolated. This value is then used whilst sweeping capOut with a matched load at port 3 to obtain the capOut value giving a peak value of 0.5 in the $|S_{31}|^2$. This should ideally be when $Q_C = 300$, yet this is not quite the case since the inability to fully de-embed the port 3 output line limits the complete removal of the contribution to Q_C of capOut when optimising capIn. This data was used to build an interpolation table that yields the required geometry needed for a filter with any desired *f*0.

There is a small section of microstrip between the feedline and "capIn", which off-resonance acts as a very short stub, which is well modelled as a parasitic capacitance to ground. An effect analogous to the impedance engineering in superconducting parametric amplifiers [10] occurs when multiple small mismatches are present along the feedline. From our simulations, to prevent the resulting stopband entering into the operational frequency band, the electrical length between filters must be suitably small ($< \lambda/4$) compared to the smallest half wavelength in the band.

4 Loss Tangent Impact

The presence of a dielectric layer introduces a loss mechanism due to parasitic two level systems (TLS), which has been extensively studied [11, 12]. The dielectric loss tangent, tanδ, is a measure of the energy dissipated through this mechanism and hence can be expressed as a quality factor and is considered to be the dominant contribution to Q_{loss} in Eq. (2) thus, $\tan\delta = 1/Q_{\text{loss}}$. Whilst there are limited published results for the loss tangent of SiN, those that are found in the literature are measured at microwave frequencies below 10 GHz [13, 14] and require a rough extrapolation of the frequency dependence up to the relevant frequencies for mm-wave astronomy. Moreover, the dielectric tanδ varies considerably depending on the deposition system and process, thus it will be crucial to characterise our SiN tanδ. For this study, we assume a SiN dielectric tanδ of 7×10^{-4} [15], since this is similar in process and device architecture.

When optimised, the maximal fraction of power, η that passes through the $\lambda/2$ filter and terminates at the detector (filter efficiency) depends on the ratio of Q_{filt} to Q_{loss} as [6]

$$\eta_{\max} = \frac{1}{2}\left[1 - \frac{Q_{\text{filt}}}{Q_{\text{loss}}}\right]^2. \tag{3}$$

Figure 2 shows the impact on η that the loss tangent has over a range of $Q_{\text{filt,lossless}}$ predicted by Eq. (3), as well as a Sonnet simulation corrected for the effective dielectric constant, which shows good agreement with a $Q_{\text{filt,lossless}} = 337$ filter at 148 GHz. There is also the expected trade-off between R and η for a given dielectric tanδ, and Fig. 2 clearly shows what stands to be gained from lower loss dielectrics such as 1×10^{-4} as is expected from amorphous silicon [2].

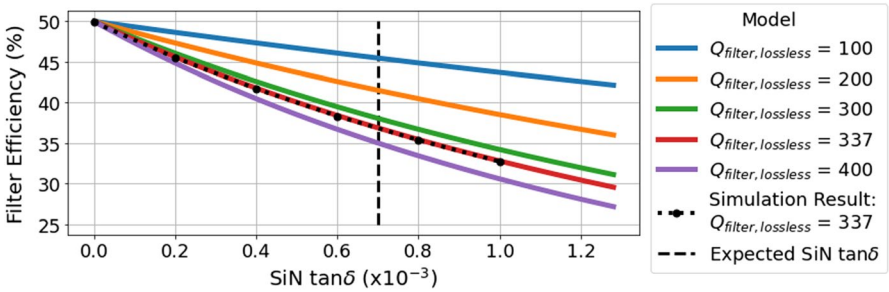

Fig. 2 (Color figure online) Trade-off between the filter resolution, R and efficiency, η for a range of initial lossless filter quality factors, $Q_{\text{filt,lossless}}$ and tanδ values. Note, to compare to the simulation, the model tanδ has been scaled by the effective dielectric constant of the inverted microstrip geometry

5 Fabrication Error Tolerance

The largest source for disagreement between simulated and fabricated filters is generally due to fabrication error, a somewhat unavoidable aspect of micro-fabrication. Deviations in the kinetic inductance, L_k, of the superconducting film, the dielectric thickness/constant, and over or under etching, have all been shown to have a considerable impact on the filter properties, and this is particularly the case for etch sensitivity with proximity-coupled filters [16]. Therefore, it is necessary to understand the tolerance of a design to a variety of fabrication errors. Figure 3 shows the filters' $Q_{\text{filt,lossless}}$ and f_0 sensitivity to variations in key features of our architecture using the python model described in Sect. 6, to study the impact of typical deposition and lithography error based on unoptimised fabrication runs at Cardiff.

These results clearly demonstrate that this design has a high tolerance to fabrication error, particularly given that worst-case errors were used. The resonant frequency is most sensitive to variations in L_k; however, this is only approximately 3.5% and suitably constant across the band. Thus, all filters should shift by the same amount. Note, changes in L_k due to a variation in niobium thickness were not considered as L_k for niobium is expected to vary slowly with thickness for $\approx$ 300-nm-thick niobium with a magnetic penetration depth of $\approx$ 135 nm. Furthermore, we see a promising forecast for the tolerance of the geometry to the variables that are the main controllers of Q_C, namely "CapIn", "CapOut", and "SiN Thickness" since these control the capacitance of the coupling capacitors, each resulting in a shift in Q between 2 and 3%. By comparison, proximity-coupled filters demonstrate a far higher sensitivity to etch error at the coupling geometry where a change in 100 nm can triple the value of Q_C [16]. This low tolerance removes the need to use electron beam lithography, a more precise but time-consuming etching method, reducing the cost and speed of device turn around.

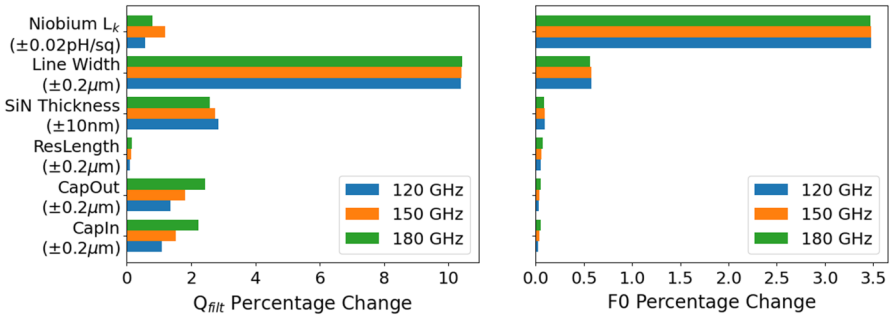

Fig. 3 (Color figure online) Simulated single-filter quality factor, Q_{filt}, (left) and resonant frequency, f_0, (right) tolerance to the worst-case fabrication errors for different variables

6 Filter-Bank Performance

Sonnet EM captures electromagnetic behaviour otherwise overlooked by lumped-element simulation software. This is at the cost of simulation run time and therefore unsuitable for simulating the performance of an FBS with more than three filters. Furthermore, niche issues start to become a problem such as larger box sizes result in dimensions that are a similar size to the signal wavelength creating interfering box modes.

We have developed a Python model based on Scikit-rf, an open-source module to create a series of cascaded lumped-element networks connected by transmission lines to simulate an N-channel filter bank. Similar methods have already been developed to simulate and analyse FBSs [17] but only from the perspective of resonator parameters, rather than using physical properties as the simulation handles, such as geometry dimensions and dielectric thickness. The model produces similar microwave responses to Sonnet by extracting the microwave component and material properties from small-scale Sonnet simulations to produce libraries for use across full, cascaded simulations. For example, the coupling capacitors were modelled as a lumped capacitance with parasitic series lumped inductances on either side with values calibrated against Sonnet simulations. A single filter typically taking ≈ 10 min to simulate in Sonnet can be simulated in $<$ 5 s. The agreement between Sonnet simulations and the python model is shown in Fig. 4. This code enabled the tolerance analysis shown in Sect. 5 and allowed us to qualitatively observe the impact the fabrication errors have on the spectral response when errors are considered across multiple interacting (over-sampled) channels.

An example of the full FBS can be seen in Fig. 5. The impact of these fabrication errors is minor compared to that of $\tan\delta = 7 \times 10^{-4}$, which accounts for much of the difference between the ideal and realistic FBS, displaying a large change in η as expected from the results seen in Sect. 4. Despite this, the FBS should still exhibit $\eta \approx 50\%$.

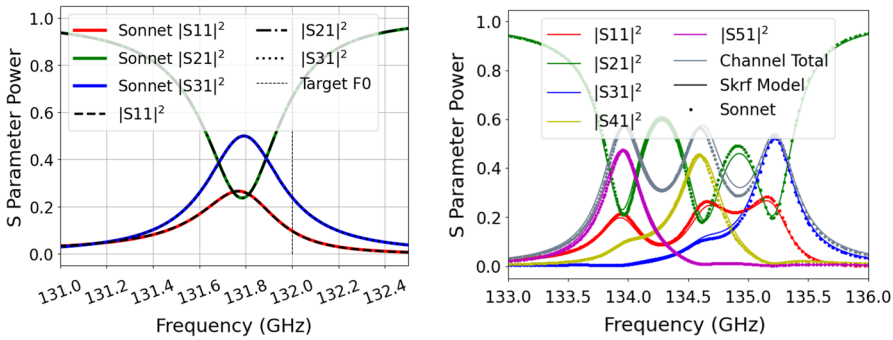

Fig. 4 (Color figure online) Comparison of the S-parameters simulated by the Scikit-rf python model to that output by Sonnet for a single filter with an intended f_0 of 132 GHz (left) and a three filter bank with $f_0 = 134.0, 134.5$ and 135.0 (right)

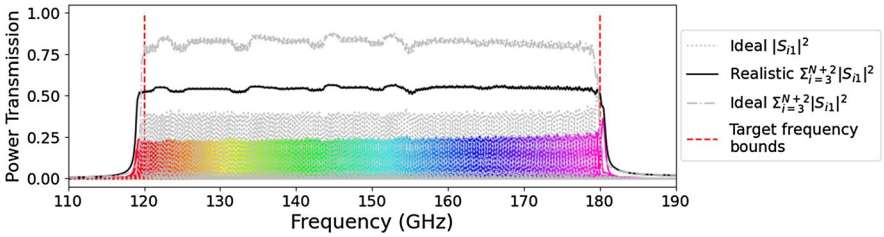

Fig. 5 (Color figure online) Two python model simulations of an SPT-SLIM filter bank between 120–180 GHz with an oversampling, $\Sigma = 1.6$ showing the single and total channel power transmission for an ideal and a realistic FBS. The colored profiles are realistic channel responses. The "Realistic" simulation includes etch error, $\tan\delta = 7 \times 10^{-4}$ and SiN thickness variation profiles over the length of the FBS based on data from unoptimised fabrication runs at Cardiff. Whereas the "Ideal" results do not include fabrication error nor loss tangent

7 Conclusion

We have presented a new filter design for a superconducting microstrip FBS and presented the optimisation process and the tolerance analysis of the design for a variety of key fabrication errors. The main differences in design compared to other FBSs [1, 2] include: the use of microstrip transmission line reducing loss by radiation loss, and parallel plate capacitor couplers at the end of each resonator rather than proximity coupling. Whilst also being a simple and easy to realise design, simulations show these filters have a high tolerance to fabrication error. The quality factor of each filter is most sensitive to variations in microstrip line widths (smallest width: 2 µm) due to over or under etching, resulting in a worst-case shift in Q_{filt} of $\approx \pm 10\%$ for a pessimistic etch uncertainty of $\pm 0.2\,\mu\text{m}$. The resonant frequency of each filter is also suitably robust, with the largest shift in f_0 of $\approx \pm 3.5\%$ being due to a ± 0.02 pH/sq deviation in the niobium kinetic inductance.

A python model, calibrated with Sonnet simulations was used to simulate the FBS and study the impact of fabrication errors on the spectral response. These simulations imply there will be limited impact on the FBS performance with a smoothly varying etch error and dielectric thickness over the wafer. Instead, improving the dielectric loss tangent is the aspect of the filter-bank design that will yield the greatest improvements in optical efficiency. For example, the lossless FBS could achieve $\eta = 80\%$, whereas with the expected SiN $\tan\delta$, we see this reduce to just under 60% in the best case.

Acknowledgements This work was supported by the members of the SPT-SLIM collaboration and made use of Scikit-rf, an open-source Python package for RF and Microwave applications. G. Robson acknowledges the continuing support from the Science and Technology Facilities Council Ph.D. studentship programme under grant reference ST/S00033X/1. We thank the reviewers who have provided insightful comments leading to improvements to this paper. The datasets generated during and/or analysed during the current study are available from the corresponding author on reasonable request.

Funding Funding was provided by Fermilab (Grant No. LDRD-2021-048), National Science Foundation (Grant No. AST-2108763) andScience and Technology Facilities Council (Grant No. GRAND NUMBER).

Open Access This article is licensed under a Creative Commons Attribution 4.0 International License, which permits use, sharing, adaptation, distribution and reproduction in any medium or format, as long as you give appropriate credit to the original author(s) and the source, provide a link to the Creative Commons licence, and indicate if changes were made. The images or other third party material in this article are included in the article's Creative Commons licence, unless indicated otherwise in a credit line to the material. If material is not included in the article's Creative Commons licence and your intended use is not permitted by statutory regulation or exceeds the permitted use, you will need to obtain permission directly from the copyright holder. To view a copy of this licence, visit http://creativecommons.org/licenses/by/4.0/.

References

1. S. Hailey-Dunsheath, E. Shirokoff, P.S. Barry, C.M. Bradford, G. Chattopadhyay, P. Day, S. Doyle, M. Hollister, A. Kovacs, H.G. LeDuc, P. Mauskopf, C.M. McKenney, R. Monroe, R. O'Brient, S. Padin, T. Reck, L. Swenson, C.E. Tucker, J. Zmuidzinas, in *Proceedings of SPIE*, vol. 9153 (2014). https://doi.org/10.1117/12.2057229
2. A. Endo, K. Karatsu, Y. Tamura, T. Oshima, A. Taniguchi, T. Takekoshi, S. Asayama, T.J.L.C. Bakx, S. Bosma, J. Bueno, K.W. Chin, Y. Fujii, K. Fujita, R. Huiting, S. Ikarashi, T. Ishida, S. Ishii, R. Kawabe, T.M. Klapwijk, K. Kohno, A. Kouchi, N. Llombart, J. Maekawa, V. Murugesan, S. Nakatsubo, M. Naruse, K. Ohtawara, A.P. Laguna, J. Suzuki, K. Suzuki, D.J. Thoen, T. Tsukagoshi, T. Ueda, P.J. de Visser, P.P. van der Werf, S.J.C. Yates, Y. Yoshimura, O. Yurduseven, J.J.A. Baselmans, Nat. Astron. **3**, 989–996 (2019). https://doi.org/10.1038/s41550-019-0850-8
3. K.S. Karkare, J. Low Temp. Phys. This Special Issue (2021)
4. P.S. Barry, J. Low Temp. Phys. This Special Issue (2021)
5. A. Kovács, P.S. Barry, C.M. Bradford, G. Chattopadhyay, P. Day, S. Doyle, S. Hailey-Dunsheath, M. Hollister, C. McKenney, H.G. LeDuc, N. Llombart, D.P. Marrone, P. Mauskopf, R.C. O'Brient, S. Padin, L.J. Swenson, J. Zmuidzinas, in *Proceedings of SPIE*, vol. 8452 (2012). https://doi.org/10.1117/12.927160
6. E. Shirokoff, P.S. Barry, C.M. Bradford, G. Chattopadhyay, P. Day, S. Doyle, S. Hailey-Dunsheath, M.I. Hollister, A. Kovács, C. McKenney, H.G. Leduc, N. Llombart, D.P. Marrone, P. Mauskopf, R. O'Brient, S. Padin, T. Reck, L.J. Swenson, J. Zmuidzinas, in *Proceedings of SPIE*, vol. 8452 (2012). https://doi.org/10.1117/12.927070
7. A. Endo, C. Sfiligoj, S.J.C. Yates, J.J.A. Baselmans, D.J. Thoen, S.M.H. Javadzadeh, P.P. van der Werf, A.M. Baryshev, T.M. Klapwijk, Appl. Phys. Lett. **103**, 032601 (2013). https://doi.org/10.1063/1.4813816
8. A. Endo, K. Karatsu, A.P. Laguna, B. Mirzaei, R. Huiting, D. Thoen, V. Murugesan, S.J.C. Yates, J. Bueno, N.V. Marrewijk, S. Bosma, O. Yurduseven, N. Llombart, J. Suzuki, M. Naruse, P.J. de Visser, P.P. van der Werf, T.M. Klapwijk, J.J.A. Baselmans, J. Astron. Telesc. Instrum. Syst. **5**(3), 035004 (2019). https://doi.org/10.1117/1.JATIS.5.3.035004
9. Sonnet Suites, Version 17.56. Accessed 2021. Available: www.sonnetsoftware.com
10. B.H. Eom, P.K. Day, H.G. LeDuc, J. Zmuidzinas. Nat. Phys. **8**, 623–627 (2012). https://doi.org/10.1038/nphys2356
11. J. Gao, PhD thesis, Department of Physics, Caltech, Pasadena, CA, USA, 2008
12. D.P. Pappas, M.R. Vissers, D.S. Wisbey, J.S. Kline, J. Gao, IEEE Trans. Appl. Supercond. **21**(3), 871–874 (2011). https://doi.org/10.1109/TASC.2010.2097578
13. J.M. Martinis, K.B. Cooper, R. McDermott, M. Steffen, M. Ansmann, K.D. Osborn, K. Cicak, S.E. Oh, D.P. Pappas, R.W. Simmonds, C.C. Yu, Phys. Rev. Lett. **95**, 210503 (2005). https://doi.org/10.1103/PhysRevLett.95.210503
14. H. Paika, K.D. Osborn, Appl. Phys. Lett. **96**, 072505 (2010). https://doi.org/10.1063/1.3309703
15. S. Hailey-Dunsheath, P.S. Barry, C.M. Bradford, G. Chattopadhyay, P. Day, S. Doyle, M. Hollister, A. Kovacs, H.G. LeDuc, N. Llombart, P. Mauskopf, C. McKenney, R. Monroe, H.T. Nguyen, R. O'Brient, S. Padin, T. Reck, E. Shirokoff, L. Swenson, C.E. Tucker, J. Zmuidzinas, J. Low Temp. Phys. **176**, 841–847 (2014). https://doi.org/10.1007/s10909-013-1068-2
16. A.P. Laguna, K. Karatsu, D. Thoen, V. Murugesan, B. Buijtendorp, A. Endo, J. Baselmans, IEEE Trans. Terahertz Sci. Technol. **11**, 635–646 (2021). https://doi.org/10.1109/TTHZ.2021.3095429

17. G. Che, PhD thesis, Department of Physics, Arizona State University, Tucson, AZ, USA, 2018

Publisher's Note Springer Nature remains neutral with regard to jurisdictional claims in published maps and institutional affiliations.